Electronic Supplementary Material (ESI) for CrystEngComm.

Supporting information.

Optical properties.

Data of IR measurements.

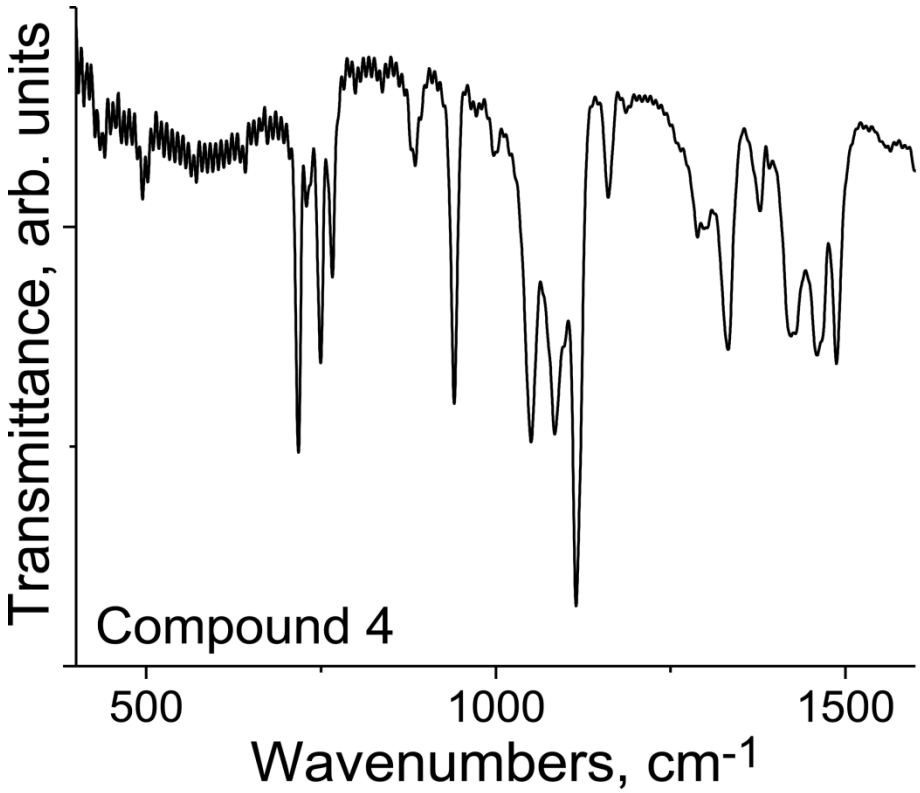

Fig. S1. IR spectrum of salt $(Pent_4N^+)\{Ti^{IV}O(Pc^{\bullet 3-})\}^{\bullet -}$ (**4**) in KBr pellet prepared in anaerobic conditions.

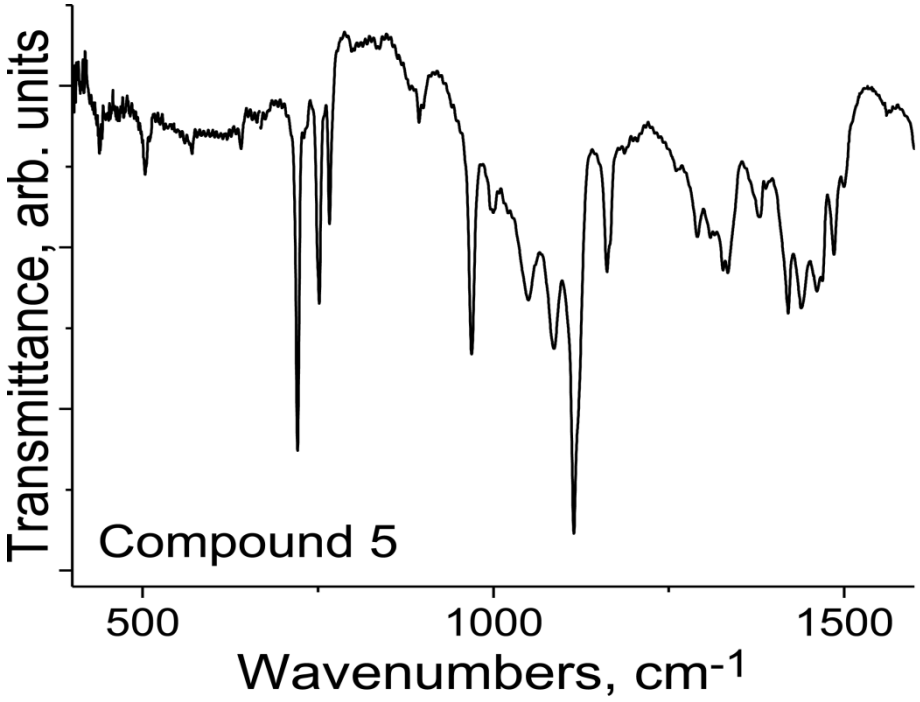

Fig. S2. IR spectrum of salt $(Pent_4N^+)\{V^{IV}O(Pc^{\bullet 3-})\}^{\bullet -}$ (**5**) in KBr pellet prepared in anaerobic conditions.

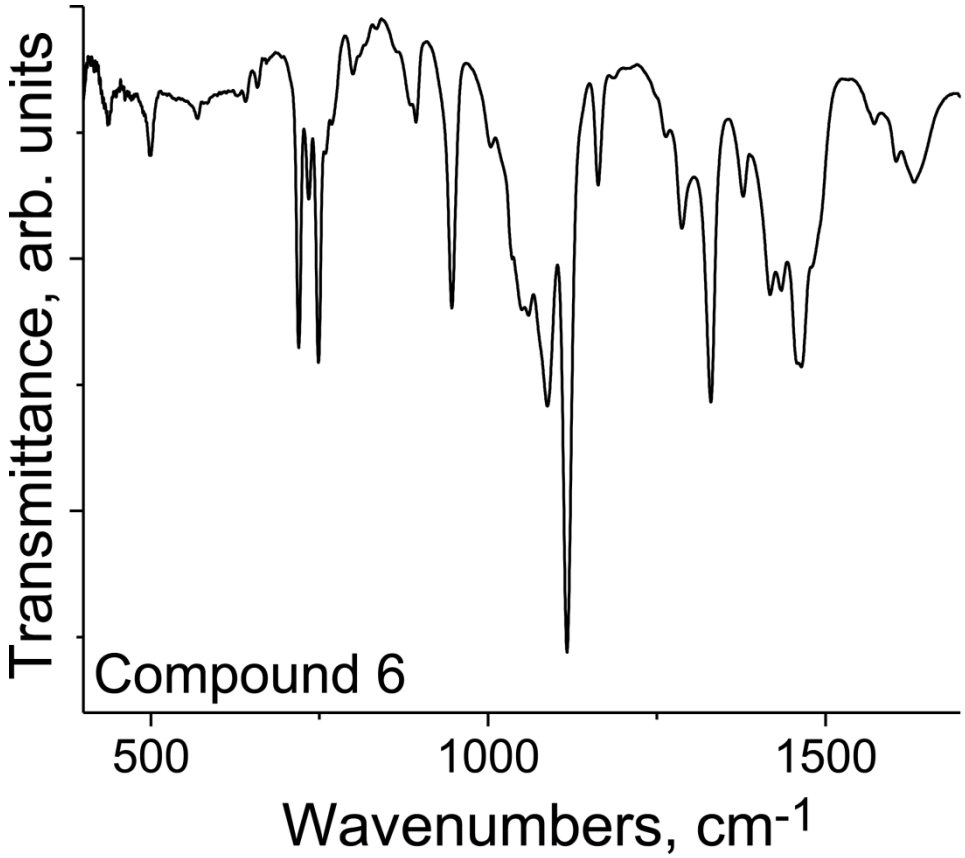

Fig. S3. IR spectrum of salt $(Hex_4N^+)\{Ti^{IV}O(Pc^{\bullet 3-})\}^{\bullet -}\cdot C_6H_4Cl_2$ (**6**) in KBr pellet prepared in anaerobic conditions.

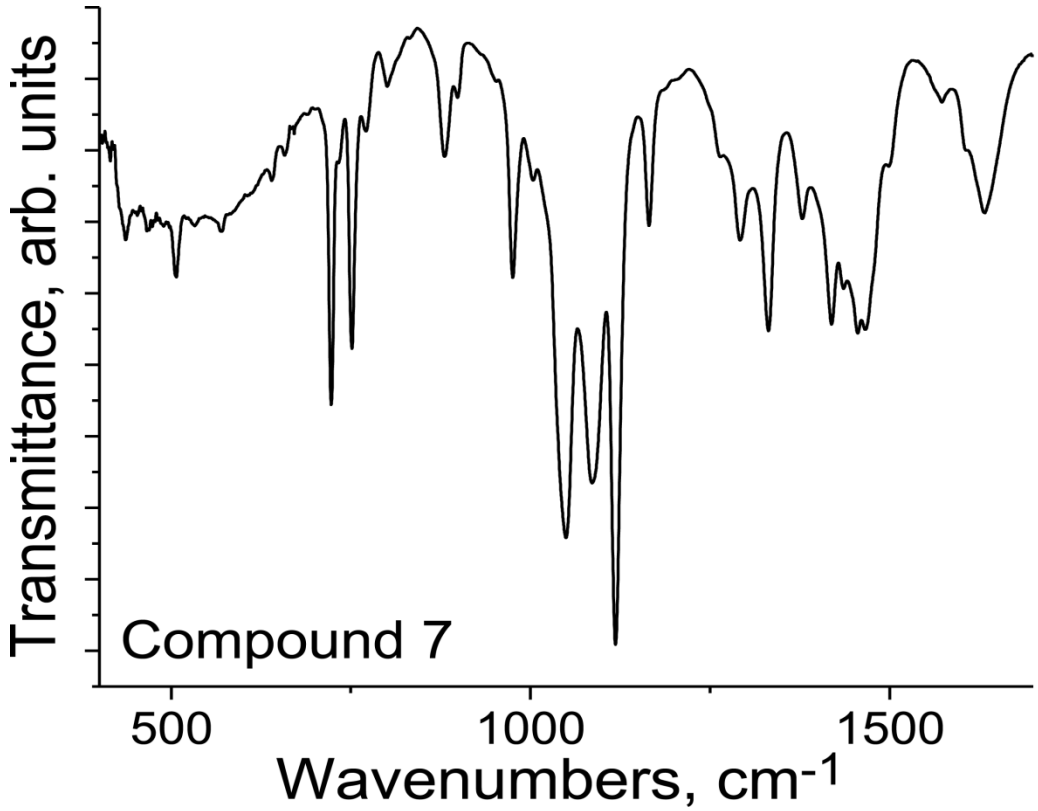

Fig. S4. IR spectrum of salt $(Hex_4N^+)\{V^{IV}O(Pc^{\bullet 3-})\}^{\bullet -}\cdot C_6H_4Cl_2$ (**7**) in KBr pellet prepared in anaerobic conditions.

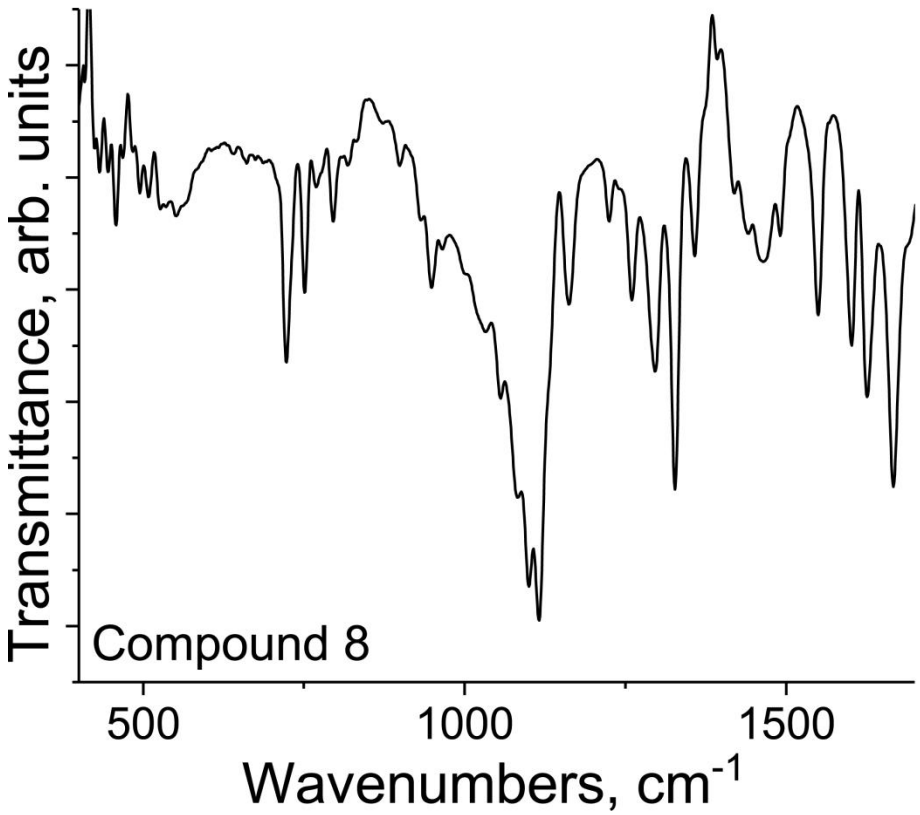

Fig. S5. IR spectrum of salt (MDABCO^{+}){Ti^{IV}O(Pc$^{\bullet 3-}$)}$^{\bullet -}$ (**8**) in KBr pellet prepared in anaerobic conditions.

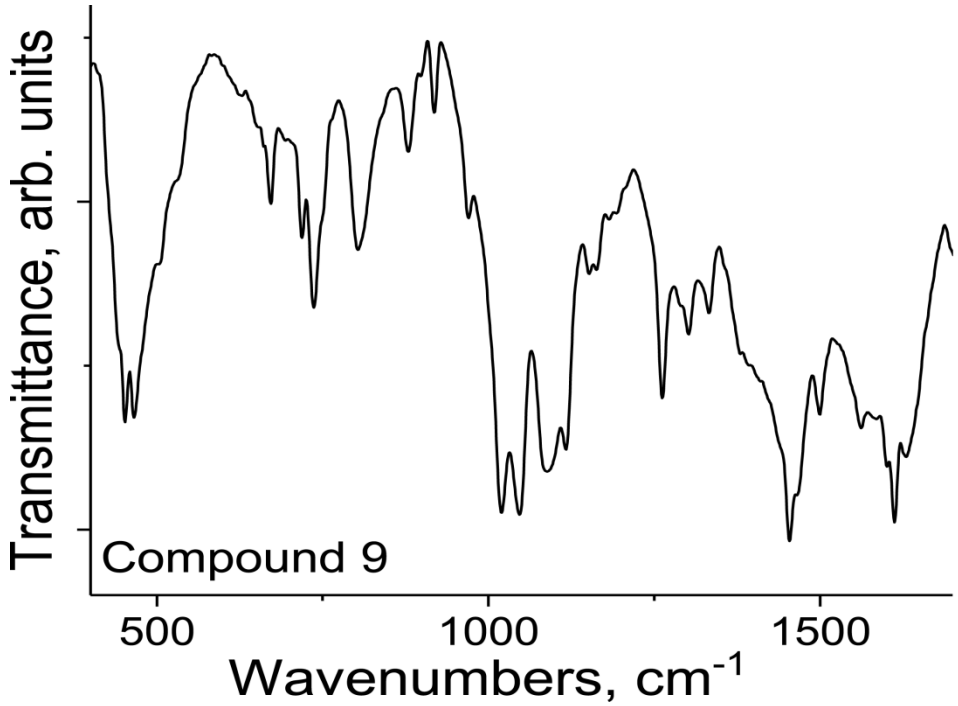

Fig. S6. IR spectrum of salt (*i*-Pr$_2$Im^{+}){M^{IV}O(Pc$^{\bullet 3-}$)}$^{\bullet -}$·0.75C$_6$H$_4$Cl$_2$ (**9**) in KBr pellet prepared in anaerobic conditions.

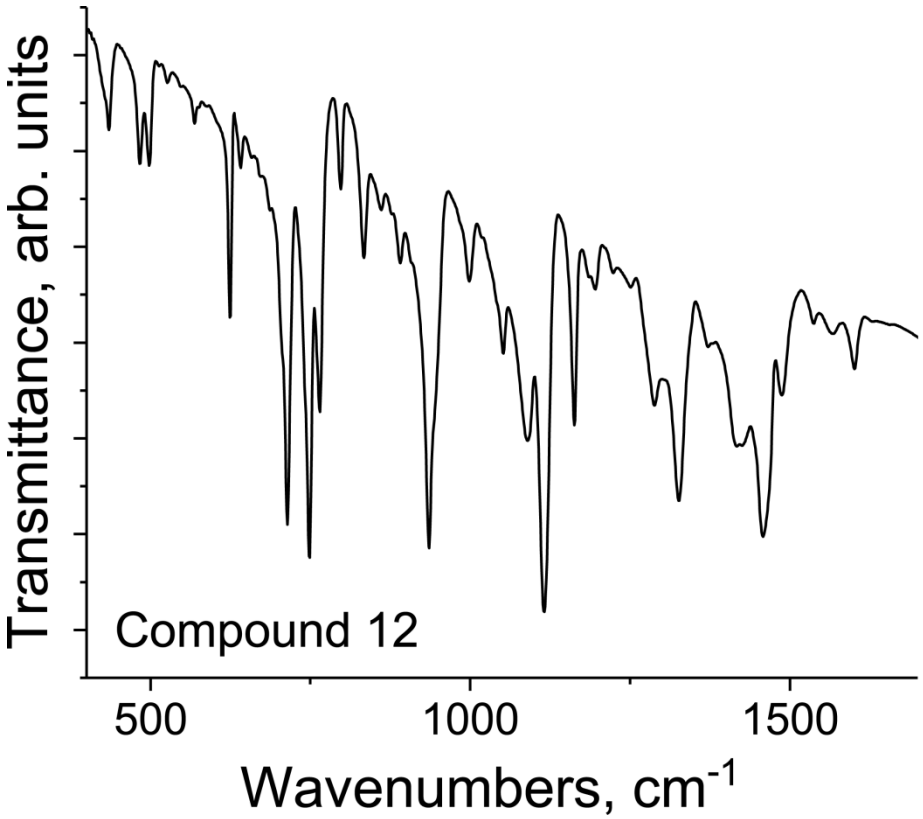

Fig. S7. IR spectrum of salt $(MDABCO^{+})(TPC)\{M^{IV}O(Pc^{\bullet 3-})\}^{\bullet -}$ (**12**) in KBr pellet prepared in anaerobic conditions.

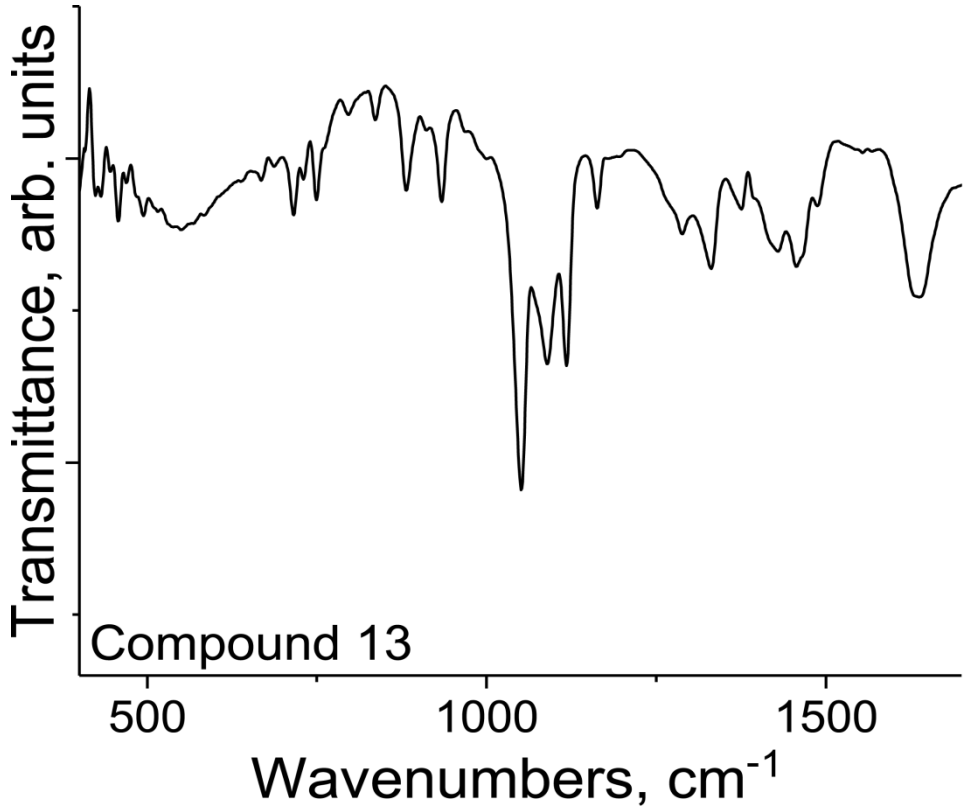

Fig. S8. IR spectrum of salt $(MDABCO^{+})_2\{Ti^{IV}O(Pc^{\bullet 3-})\}^{\bullet -}(I^{-})$ (**13**) in KBr pellet prepared in anaerobic conditions.

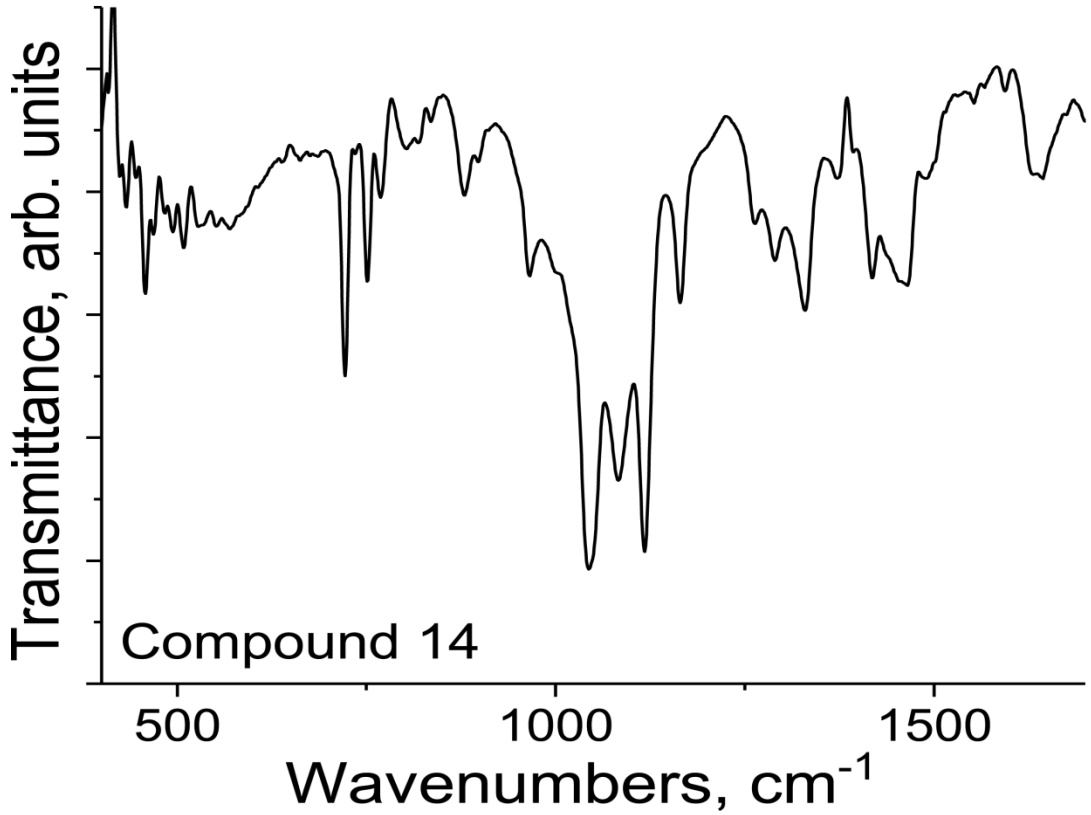

Fig. S9. IR spectrum of salt $(MDABCO^{+})_2\{V^{IV}O(Pc^{\bullet 3-})\}^{\bullet -}(I^{-})$ (**14**) in KBr pellet prepared in anaerobic conditions.

Spectra of the salts in the UV-visible-NIR ranges.

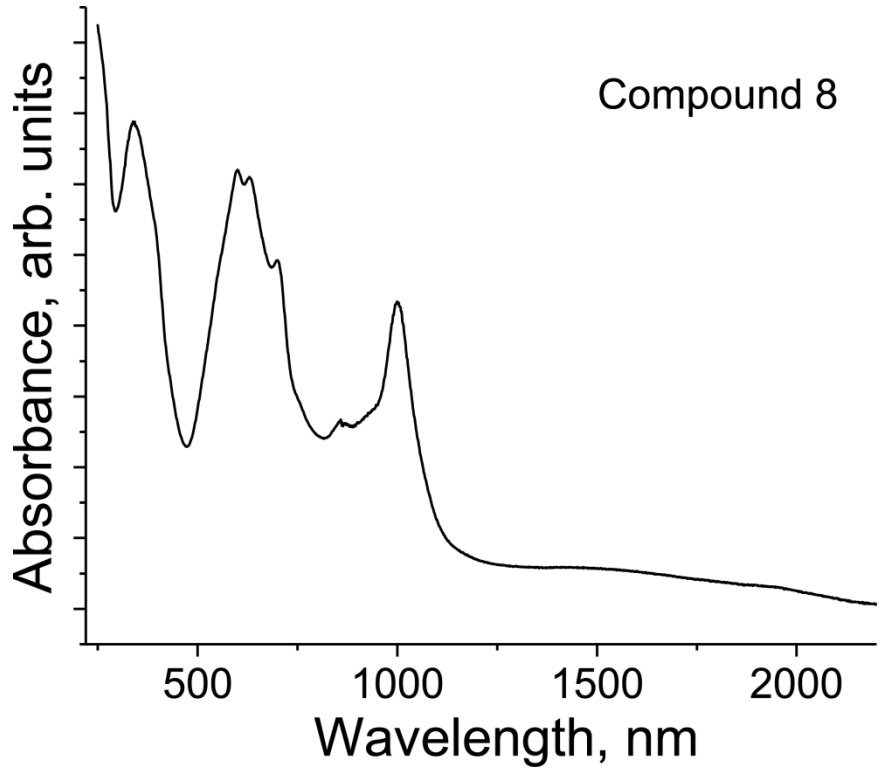

Fig. S10. Spectrum of salt (MDABCO^{+}){Ti^{IV}O(Pc$^{\bullet 3-}$)}$^{\bullet -}$ (**8**) in the UV-visible-NIR ranges in KBr pellet prepared in anaerobic conditions.

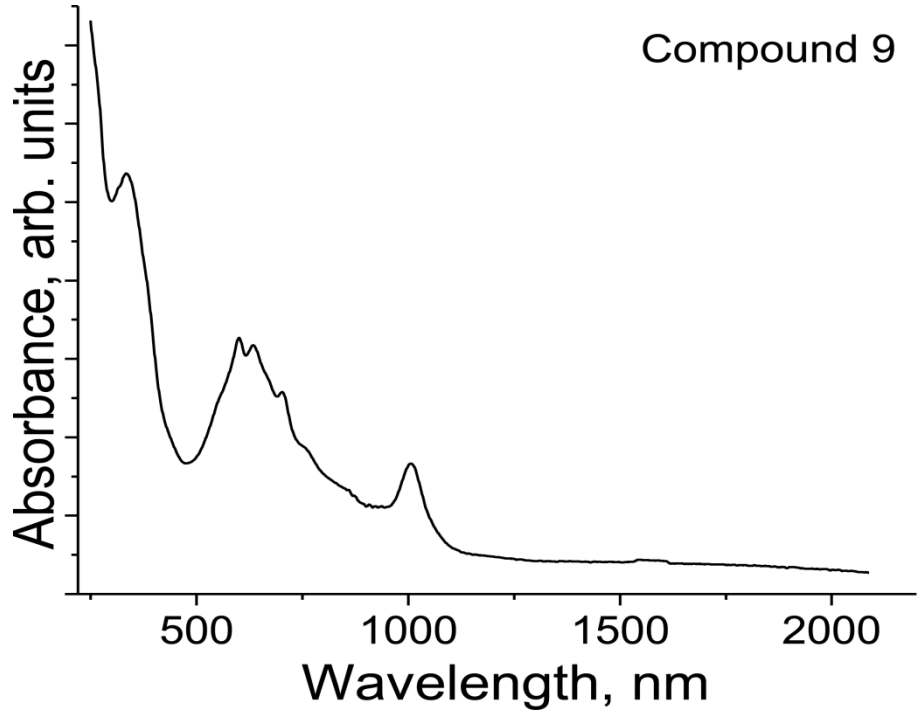

Fig. S11. Spectrum of salt (*i*-Pr$_2$Im^{+}){M^{IV}O(Pc$^{\bullet 3-}$)}$^{\bullet -}$·0.75C$_6$H$_4$Cl$_2$ (**9**) in the UV-visible-NIR ranges in KBr pellet prepared in anaerobic conditions.

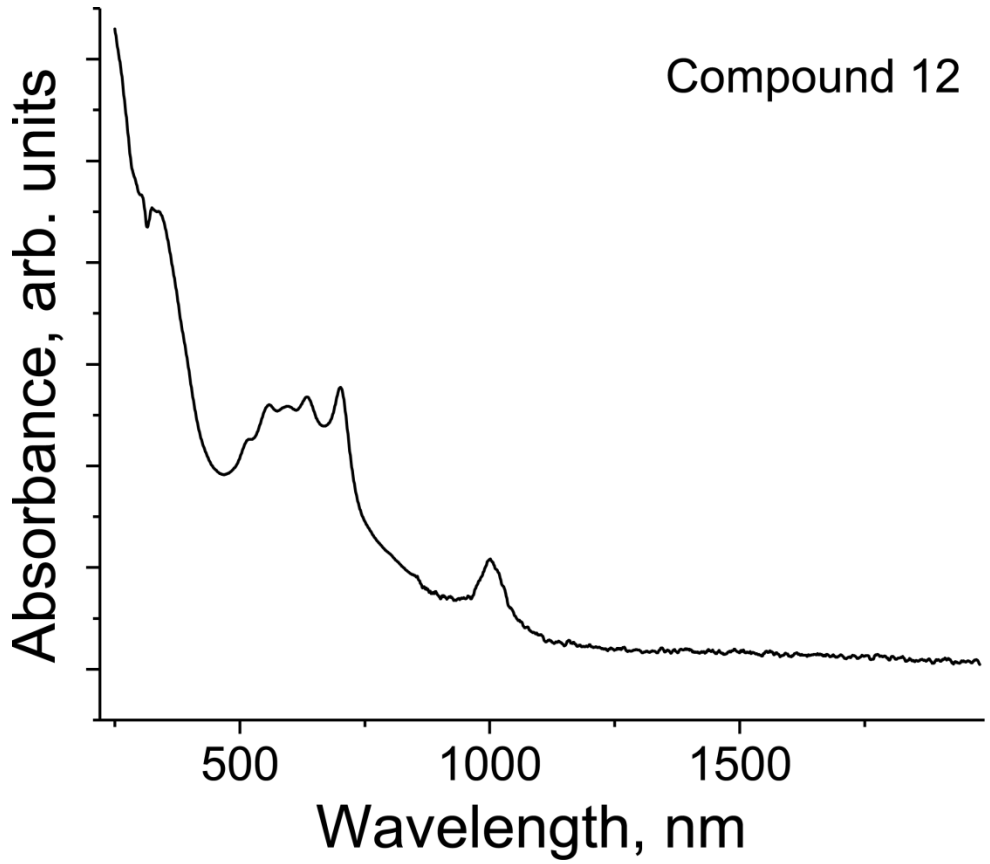

Fig. S12. Spectrum of salt $(MDABCO^{+})(TPC)\{M^{IV}O(Pc^{\bullet 3-})\}^{\bullet -}$ (**12**) in the UV-visible-NIR ranges in KBr pellet prepared in anaerobic conditions.

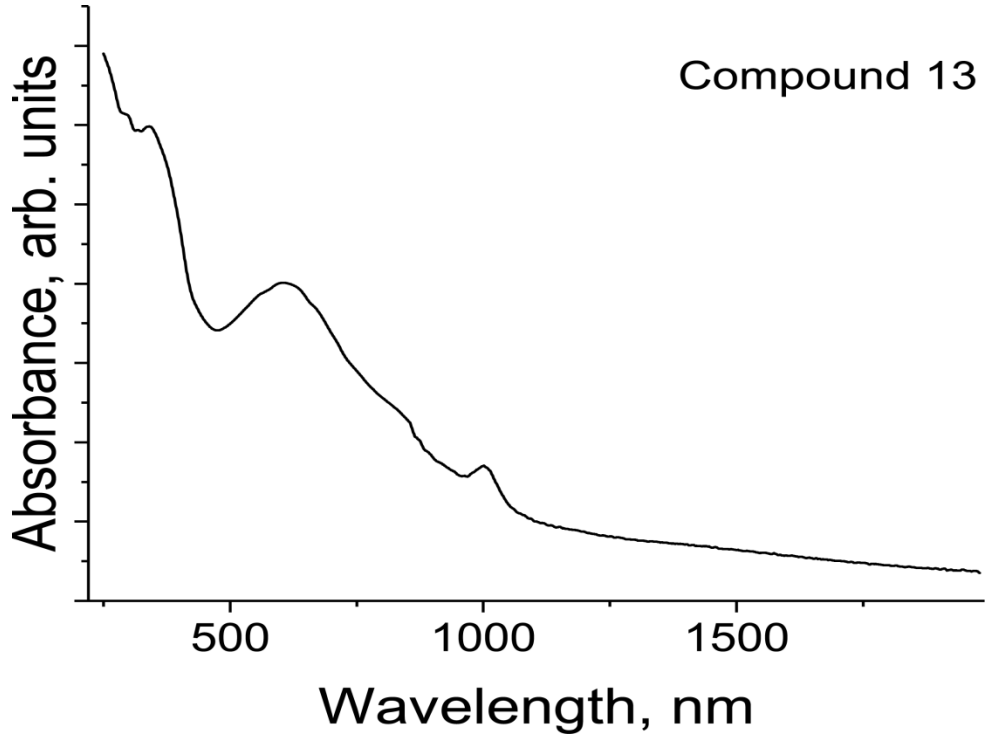

Fig. S13. Spectrum of salt $(MDABCO^{+})_2\{Ti^{IV}O(Pc^{\bullet 3-})\}^{\bullet -}(I^{-})$ (**13**) in the UV-visible-NIR ranges in KBr pellet prepared in anaerobic conditions.

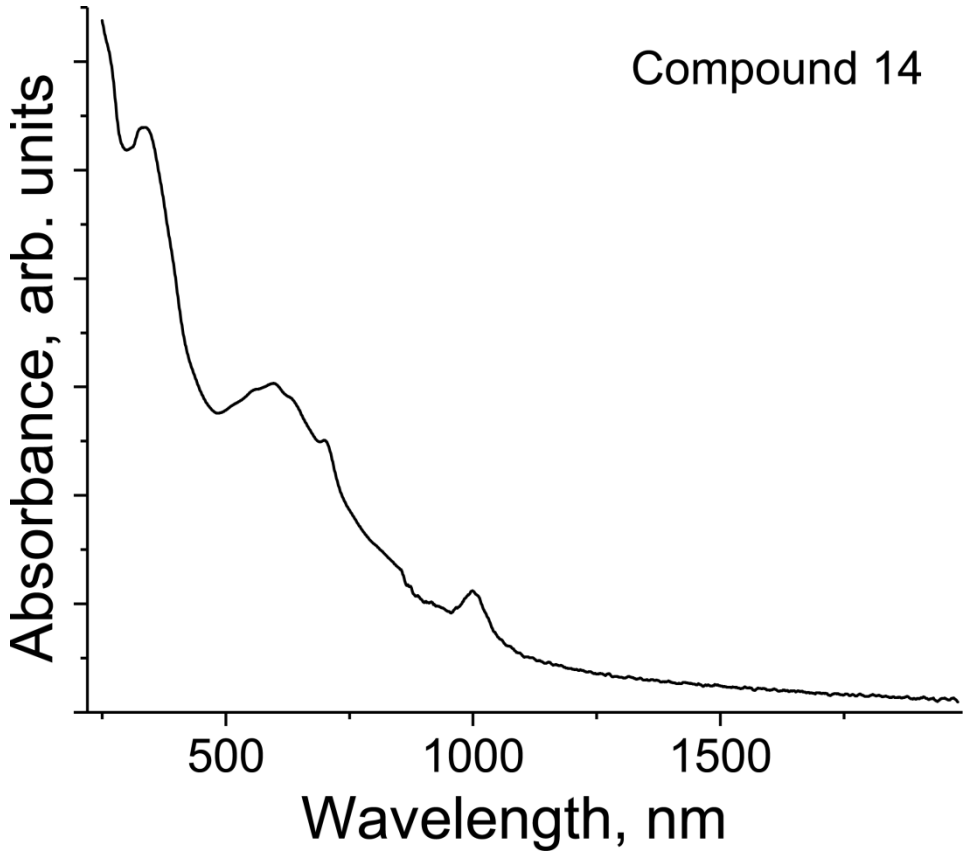

Fig. S14. Spectrum of salt $(MDABCO^{+})_2\{V^{IV}O(Pc^{\bullet 3-})\}^{\bullet -}(I^{-})$ (**14**) in the UV-visible-NIR ranges in KBr pellet prepared in anaerobic conditions.

Magnetic properties.

SQUID data.

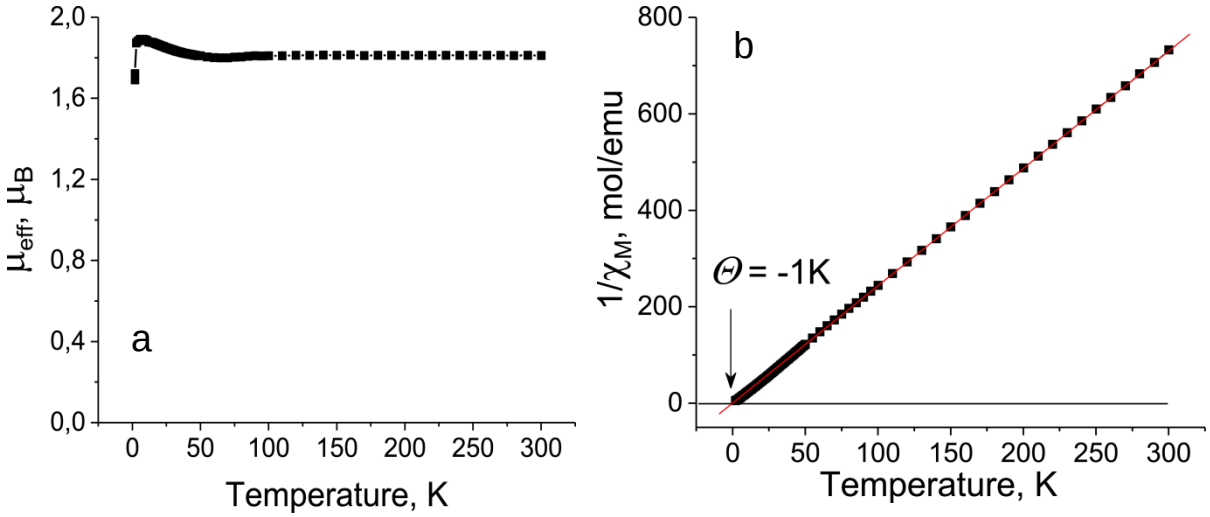

Figure S15. Temperature dependence of effective magnetic moment (a) and reciprocal molar magnetic susceptibility (b) of polycrystalline sample of $(Pent_4N^+)\{Ti^{IV}O(Pc^{\bullet 3-})\}^{\bullet -}$ (**4**).

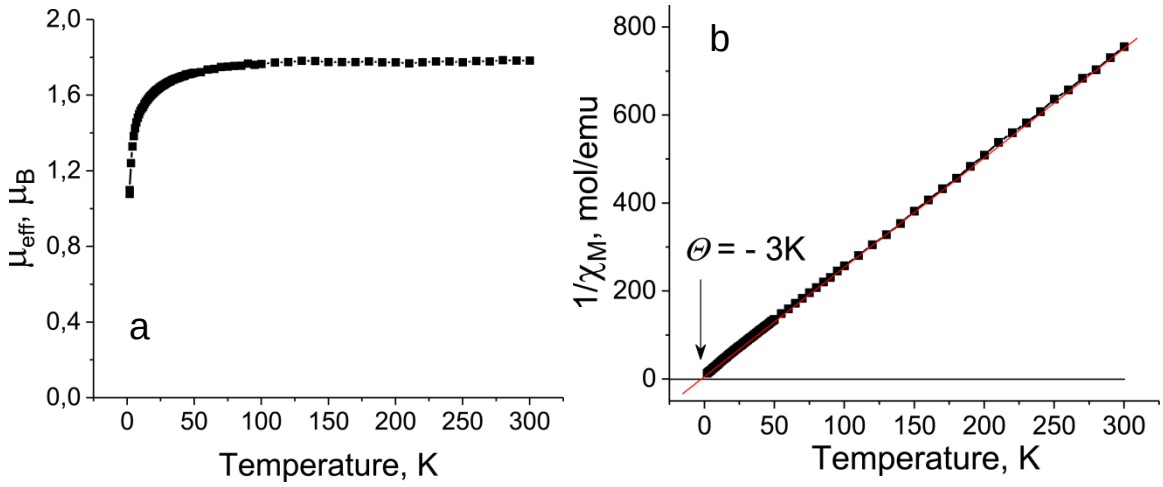

Figure S16. Temperature dependence of effective magnetic moment (a) and reciprocal molar magnetic susceptibility (b) of polycrystalline sample of $(Hex_4N^+)\{Ti^{IV}O(Pc^{\bullet 3-})\}^{\bullet -}\cdot C_6H_4Cl_2$ (**6**).

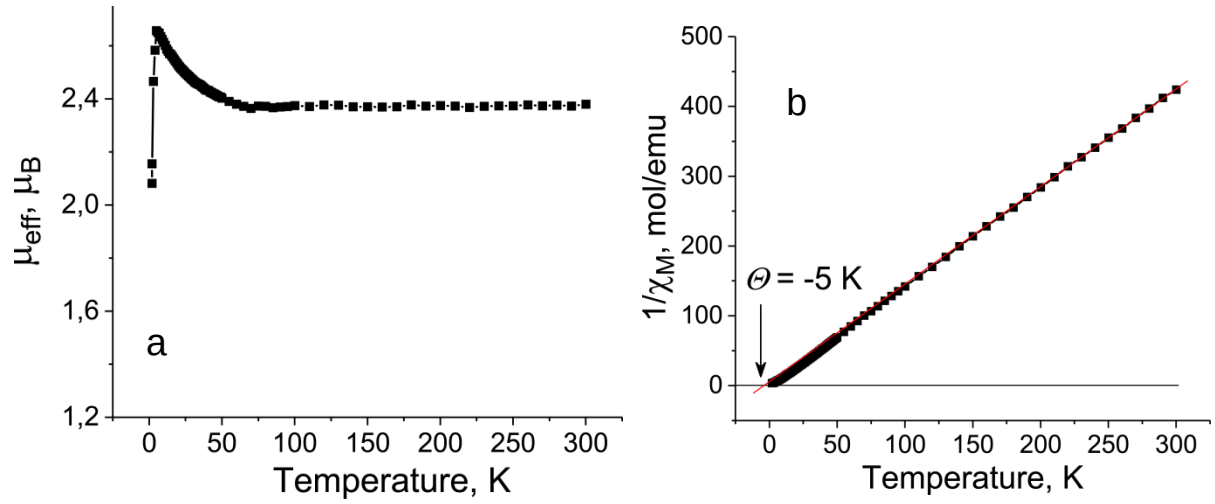

Figure S17. Temperature dependence of effective magnetic moment (a) and reciprocal molar magnetic susceptibility (b) of polycrystalline sample of $(Pent_4N^+)\{V^{IV}O(Pc^{\bullet 3-})\}^{\bullet -}$ (**5**).

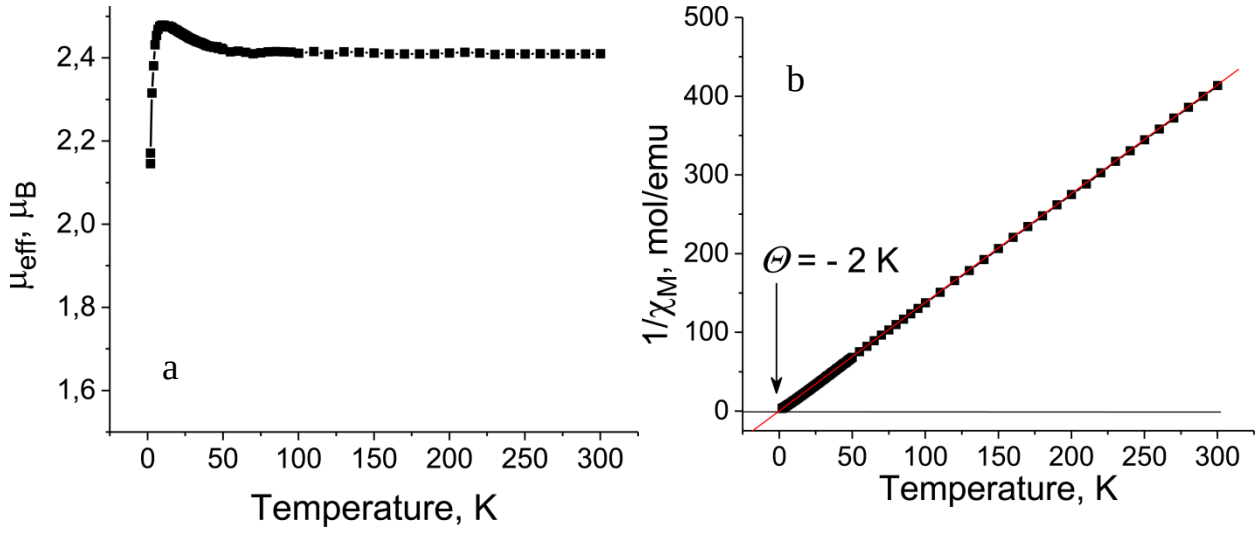

Figure S18. Temperature dependence of effective magnetic moment (a) and reciprocal molar magnetic susceptibility (b) of polycrystalline sample of $(Hex_4N^+)\{V^{IV}O(Pc^{\bullet 3-})\}^{\bullet -}\cdot C_6H_4Cl_2$ (**7**).

EPR data.

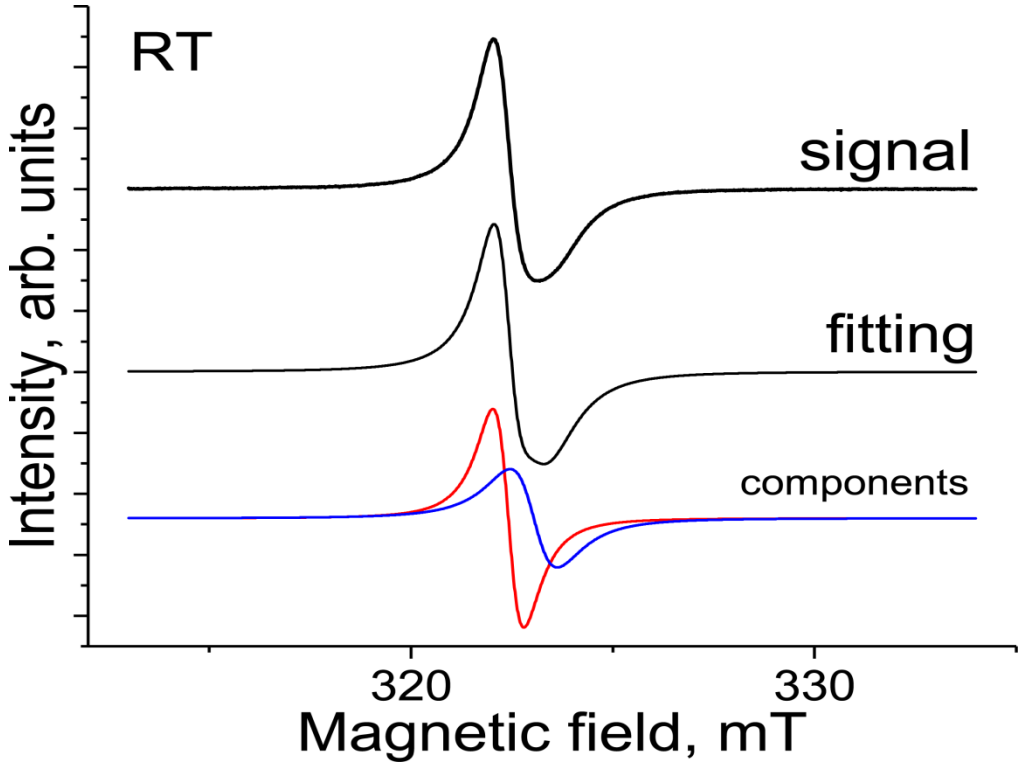

Fig. S19. EPR spectrum of polycrystalline salt $(Pent_4N^+)\{Ti^{IV}O(Pc^{\bullet 3-})\}^{\bullet -}$ (**4**) at room temperature. Fitting of the signal by two Lorentzian lines is shown in middle and bottom.

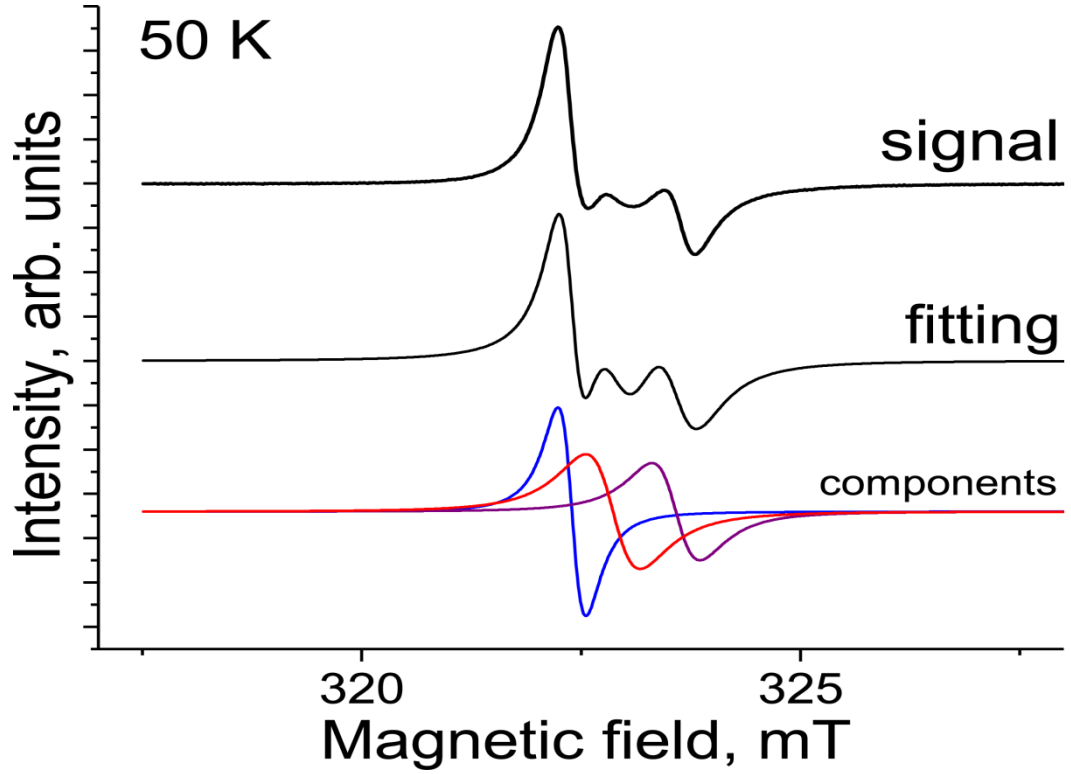

Fig. S20. EPR spectrum of polycrystalline salt $(Pent_4N^+)\{Ti^{IV}O(Pc^{\bullet 3-})\}^{\bullet -}$ (**4**) at 50 K. Fitting of the signal by three Lorentzian lines is shown in middle and bottom.

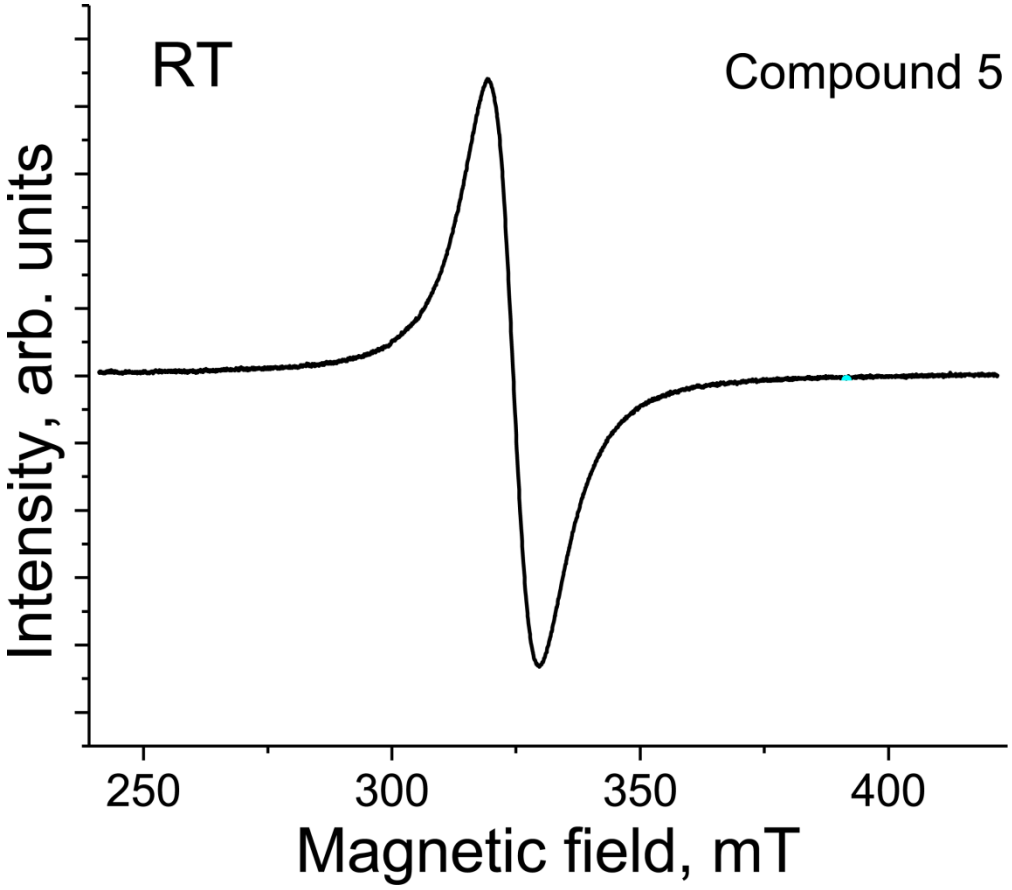

Fig. S21. EPR spectrum of polycrystalline salt $(Pent_4N^+)\{V^{IV}O(Pc^{\bullet 3-})\}^{\bullet -}$ (**5**) at room temperature.

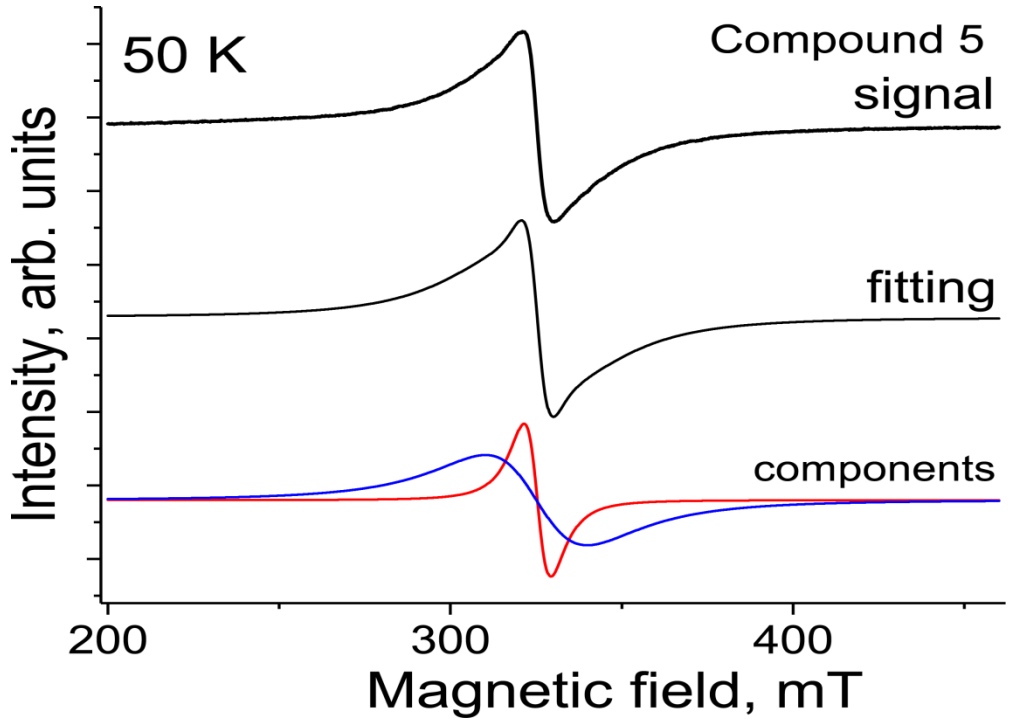

Fig. S21. EPR spectrum of polycrystalline salt $(Pent_4N^+)\{V^{IV}O(Pc^{\bullet 3-})\}^{\bullet -}$ (**5**) at 50 K. Fitting of the signal by two Lorentzian lines is shown in middle and bottom.

.

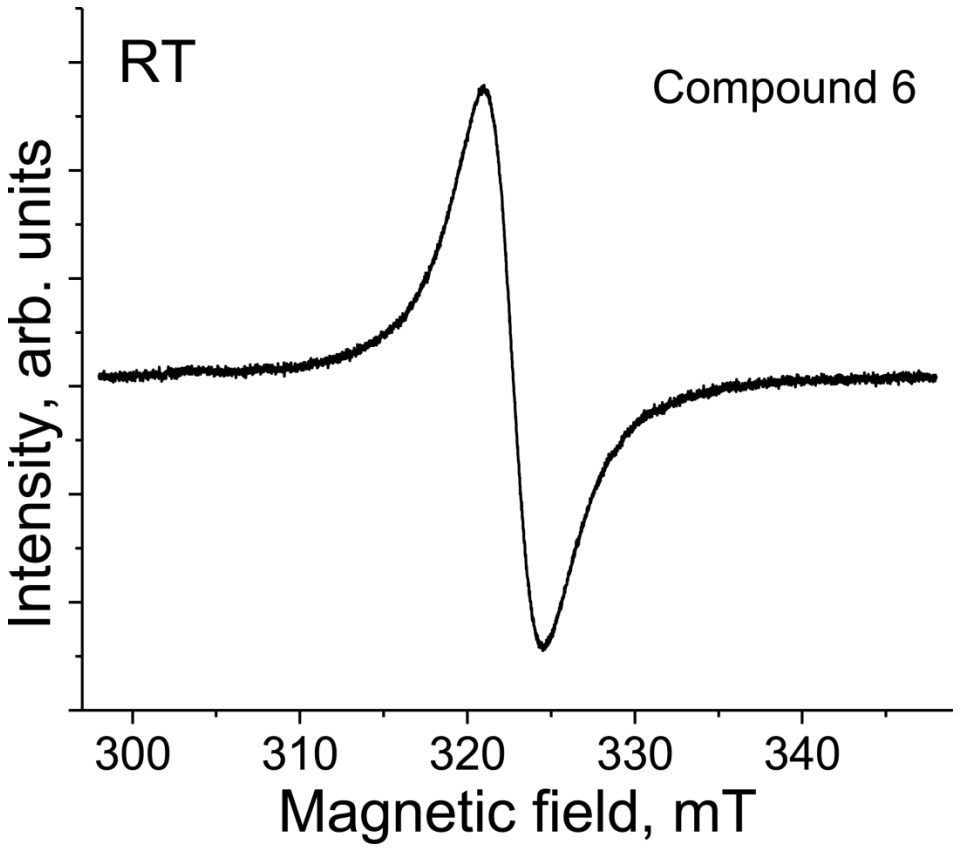

Fig. S22. EPR spectrum of polycrystalline salt $(Hex_4N^+)\{Ti^{IV}O(Pc^{\bullet 3-})\}^{\bullet -}\cdot C_6H_4Cl_2$ (**6**) at room temperature.

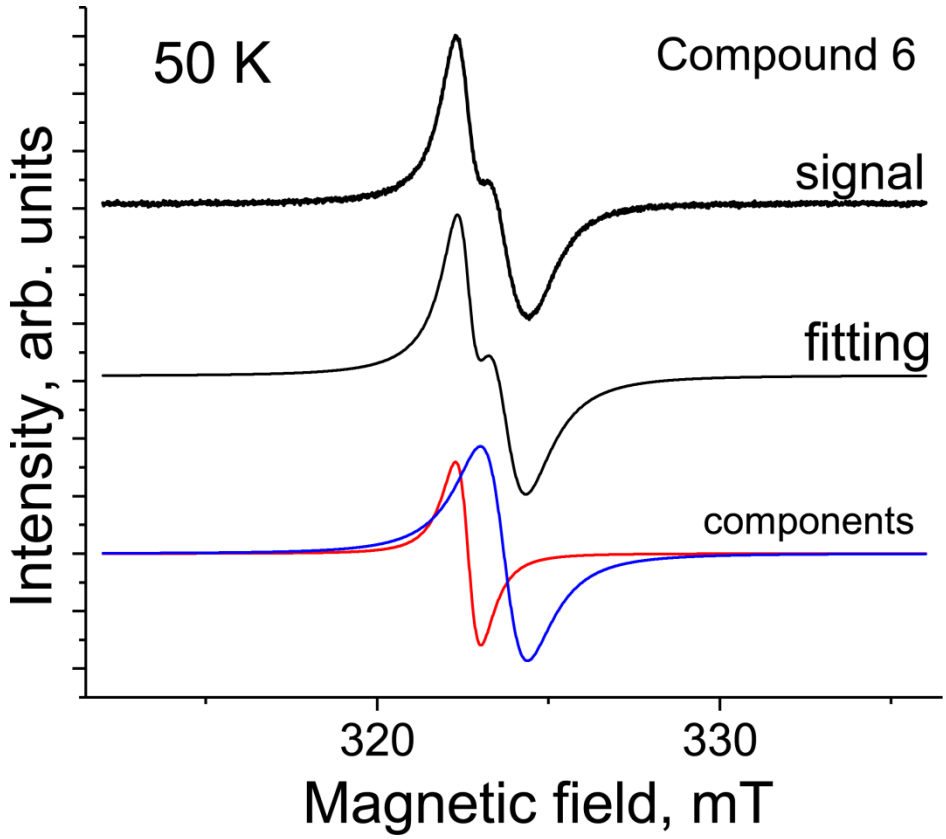

Fig. S23. EPR spectrum of polycrystalline salt $(Hex_4N^+)\{Ti^{IV}O(Pc^{\bullet 3-})\}^{\bullet -}\cdot C_6H_4Cl_2$ (**6**) at 50 K. Fitting of the signal by two Lorentzian lines is shown in middle and bottom.

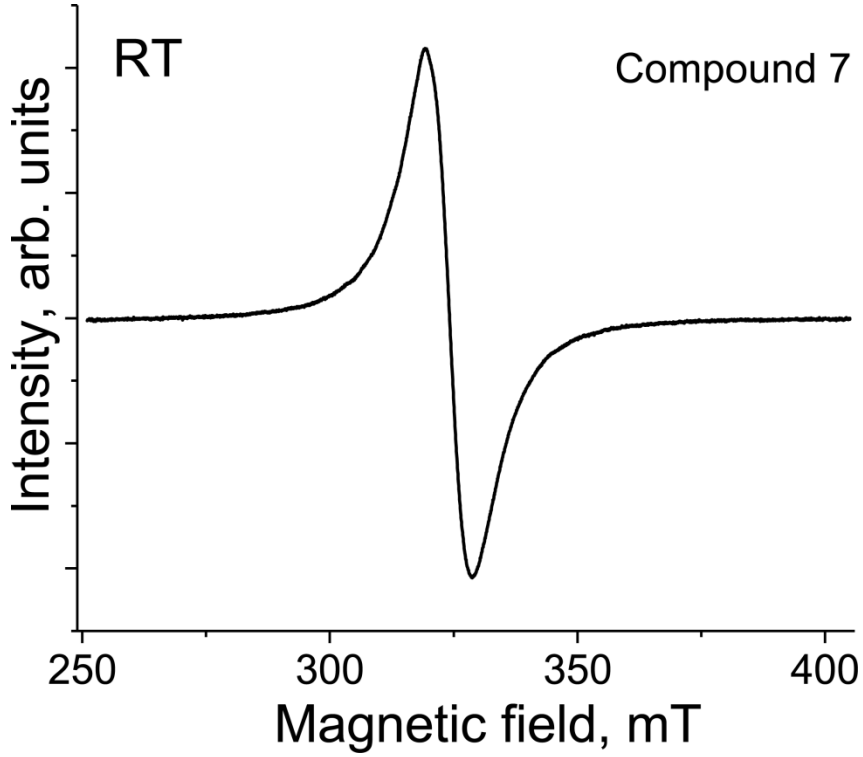

Fig. S24. EPR spectrum of polycrystalline salt $(Hex_4N^+)\{V^{IV}O(Pc^{\bullet 3-})\}^{\bullet -}\cdot C_6H_4Cl_2$ (**7**) at room temperature.

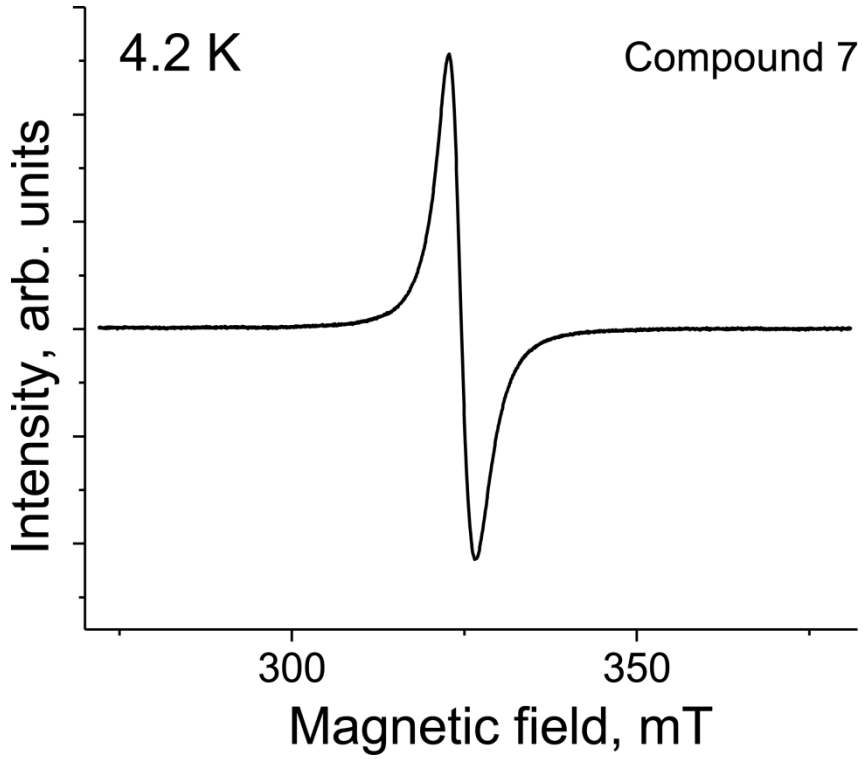

Fig. S25. EPR spectrum of polycrystalline salt $(Hex_4N^+)\{V^{IV}O(Pc^{\bullet 3-})\}^{\bullet -}\cdot C_6H_4Cl_2$ (**7**) at 4.2 K.

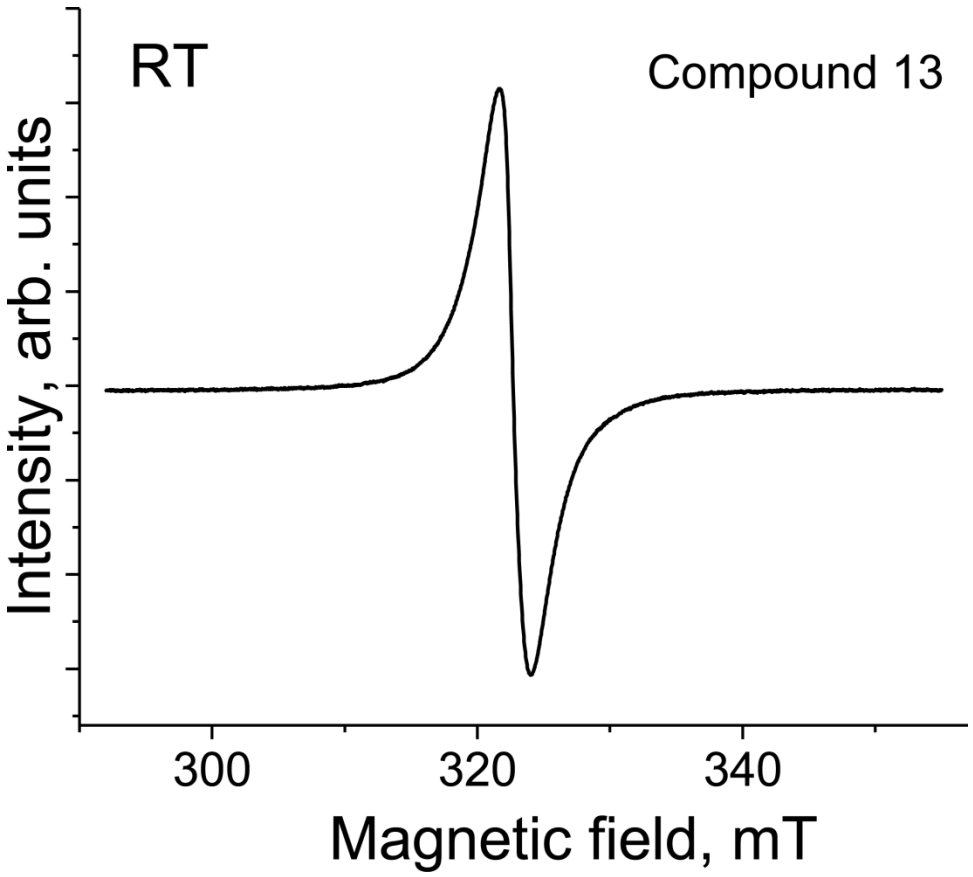

Fig. S26. EPR spectrum of polycrystalline salt $(MDABCO^{+})_2\{Ti^{IV}O(Pc^{\bullet 3-})\}^{\bullet -}(I^{-})$ (**13**) at room temperature.

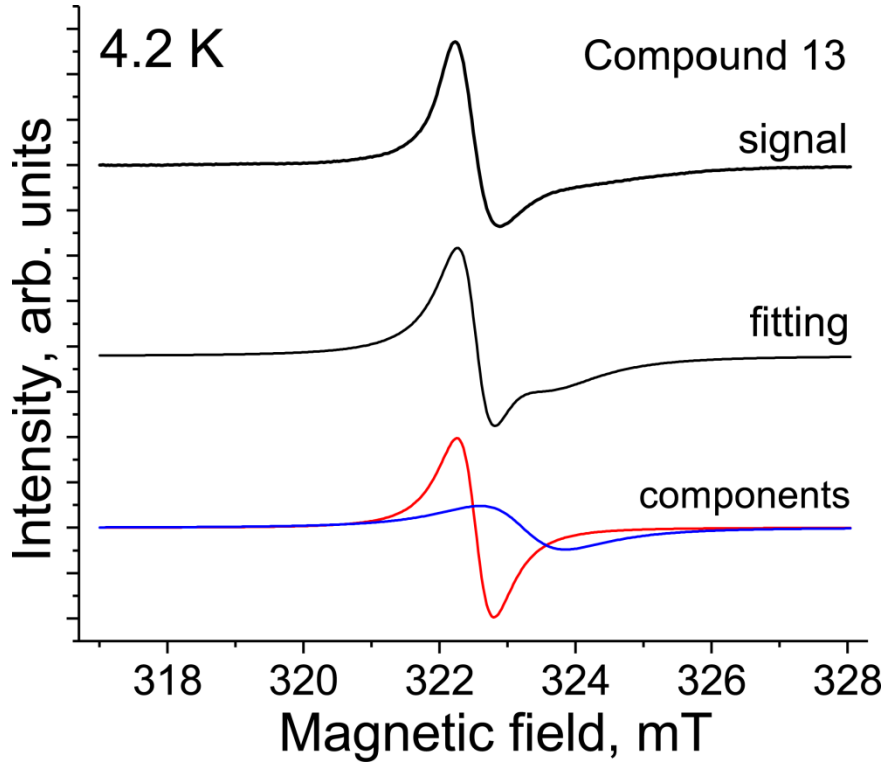

Fig. S27. EPR spectrum of polycrystalline salt $(MDABCO^{+})_2\{Ti^{IV}O(Pc^{\bullet 3-})\}^{\bullet -}(I^{-})$ (**13**) at 4.2 K. Fitting of the signal by two Lorentzian lines is shown in middle and bottom.

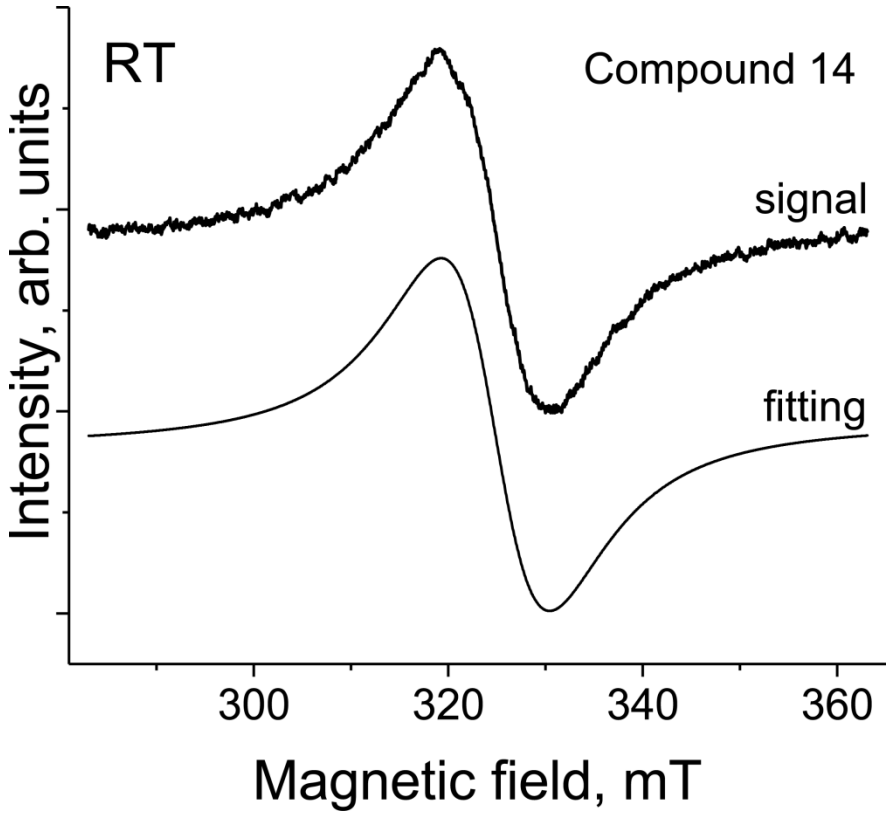

Fig. S28. EPR spectrum of polycrystalline salt $(MDABCO^{+})_2\{V^{IV}O(Pc^{\bullet 3-})\}^{\bullet -}(I^{-})$ (**14**) at room temperature. Fitting of the signal by one Lorentzian line is shown bottom.

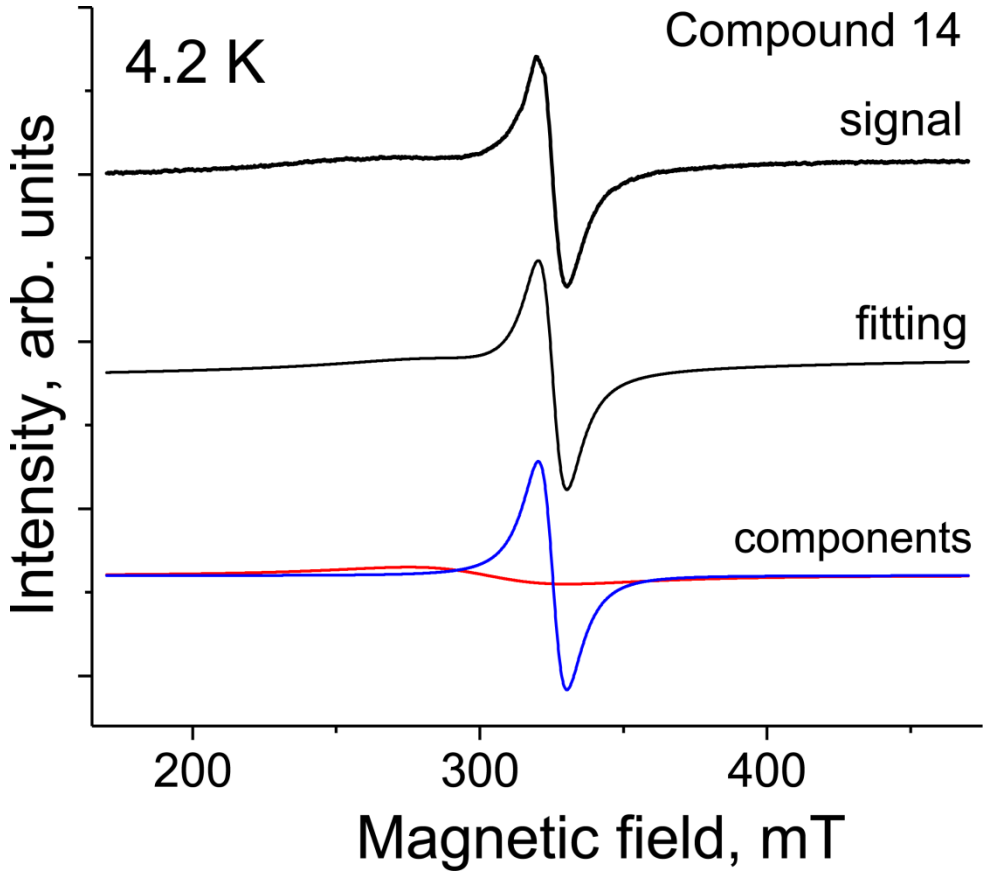

Fig. S29. EPR spectrum of polycrystalline salt $(MDABCO^{+})_2\{V^{IV}O(Pc^{\bullet 3-})\}^{\bullet -}(I^{-})$ (**14**) at 4.2 K. Fitting of the signal by two Lorentzian lines is shown in middle and bottom.

Crystal structure data.

Packing of the salts.

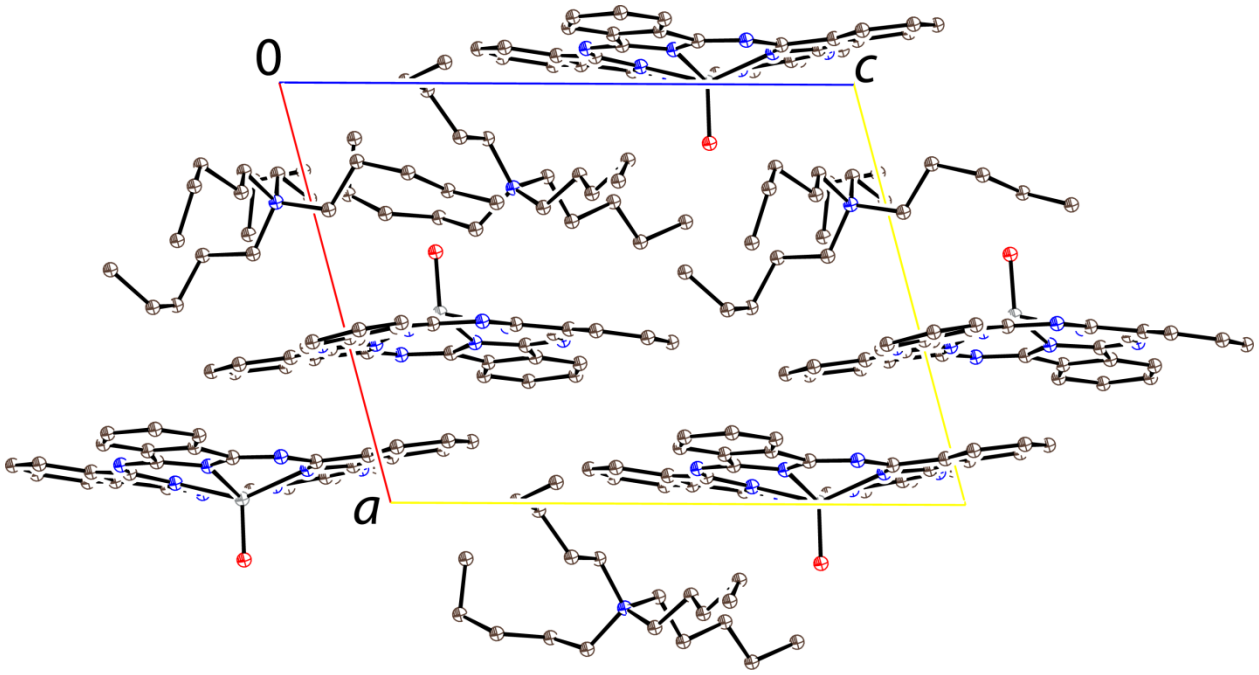

Fig. S30. View on the unit cell of salt $(Pent_4N^+)\{Ti^{IV}O(Pc^{\bullet 3-})\}^{\bullet -}$ (**4**) along the crystallographic *b* axis.

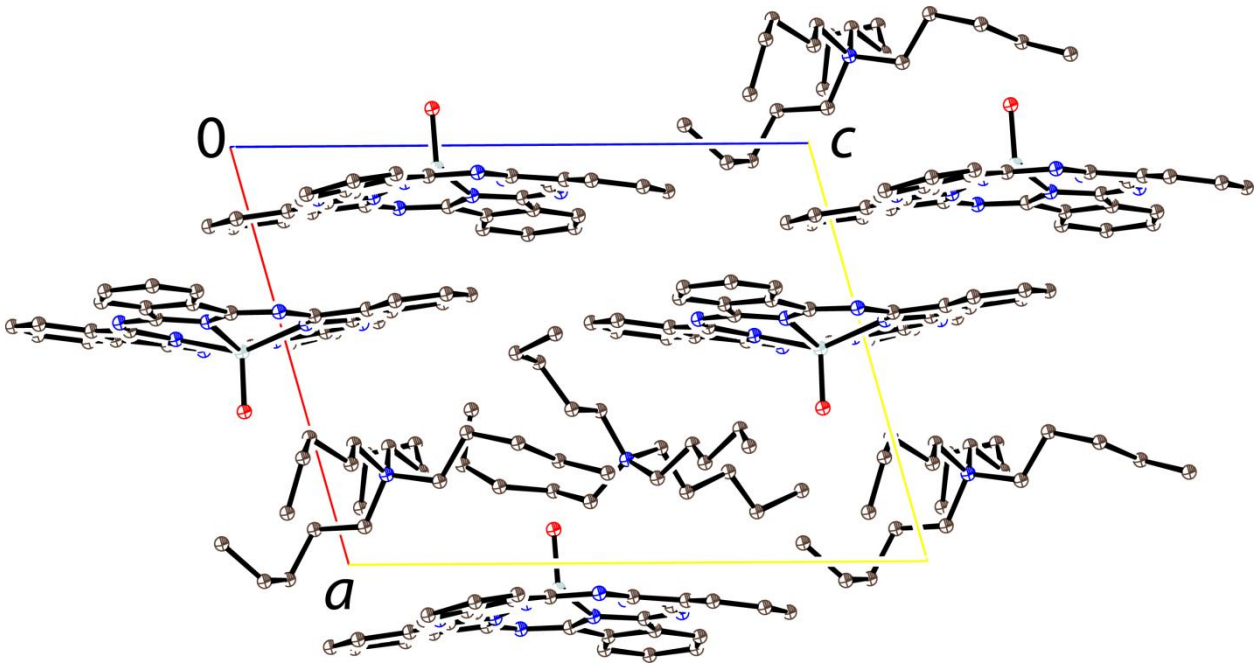

Fig. S31. View on the unit cell of salt $(Pent_4N^+)\{V^{IV}O(Pc^{\bullet 3-})\}^{\bullet -}$ (**5**) along the crystallographic *b* axis.

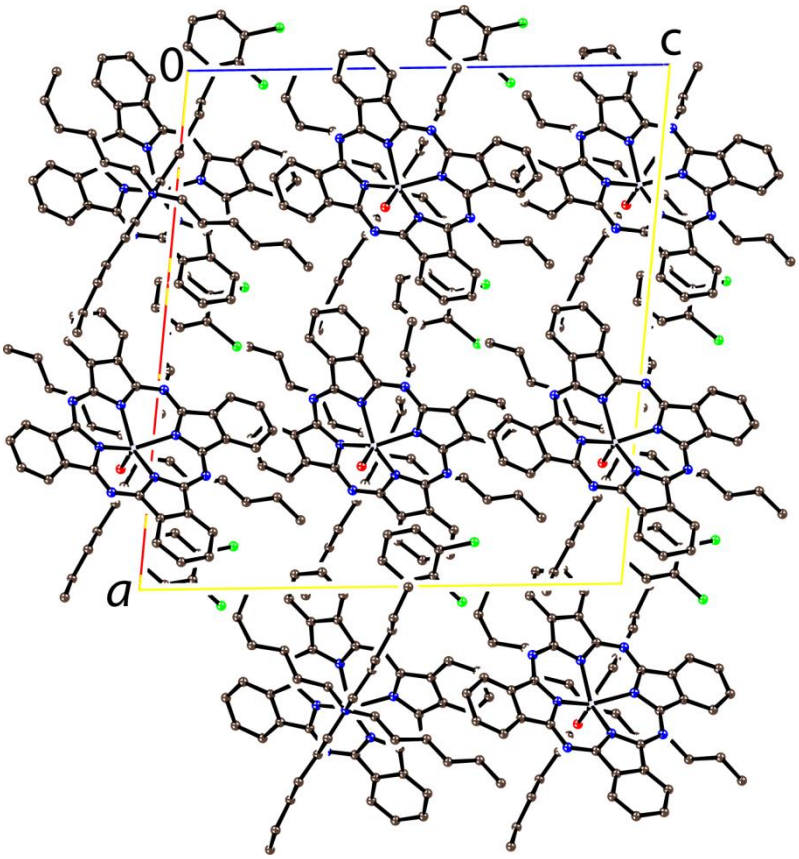

Fig. S32. View on the unit cell of salt $(Hex_4N^+)\{Ti^{IV}O(Pc^{\bullet 3-})\}^{\bullet -}$ (**6**) along the crystallographic *b* axis.

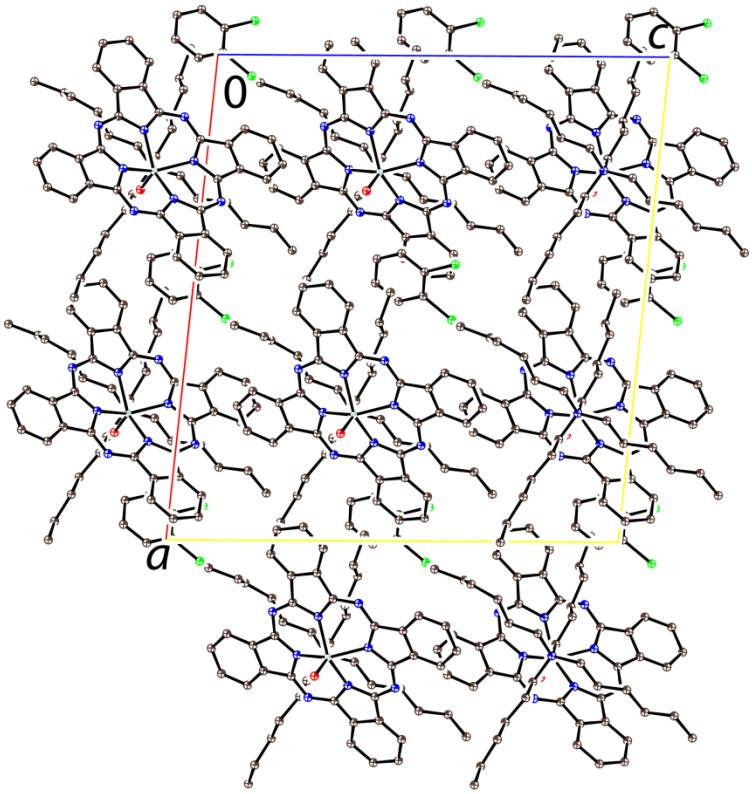

Fig. S33. View on the unit cell of salt $(Hex_4N^+)\{V^{IV}O(Pc^{\bullet 3-})\}^{\bullet -}$ (**7**) along the crystallographic *b* axis.

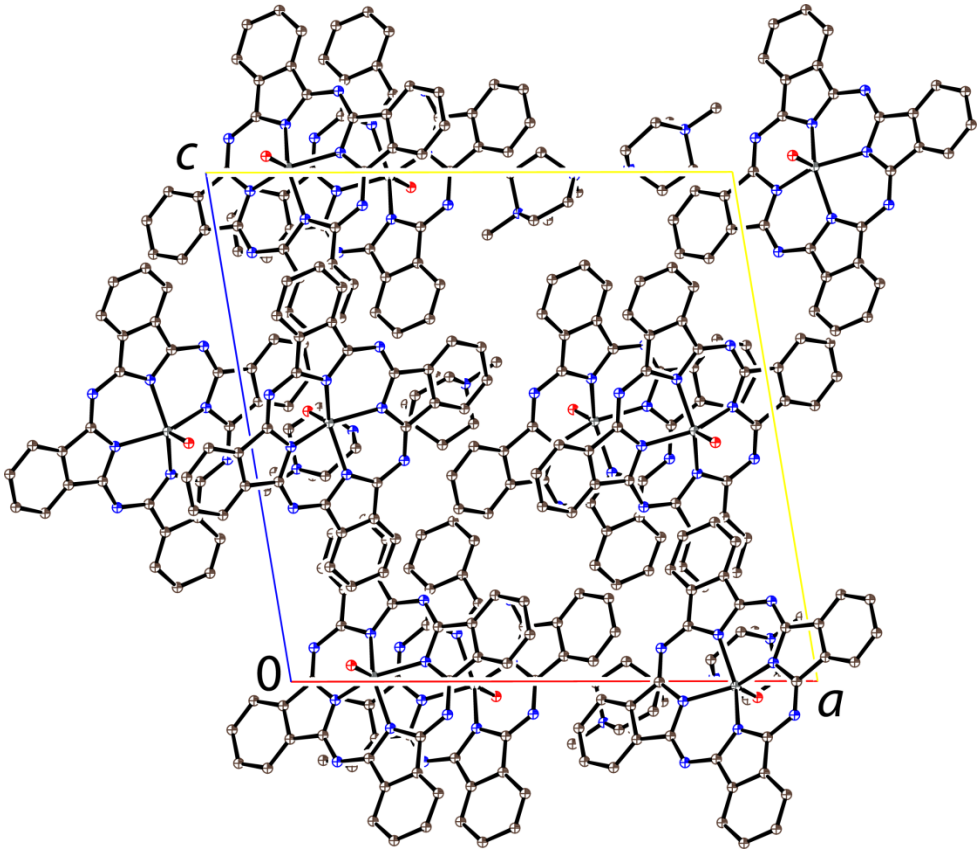

Fig. S34. View on the unit cell of salt $(MDABCO^{+})\{Ti^{IV}O(Pc^{\bullet 3-})\}^{\bullet -}$ (**8**) along the crystallographic *b* axis.

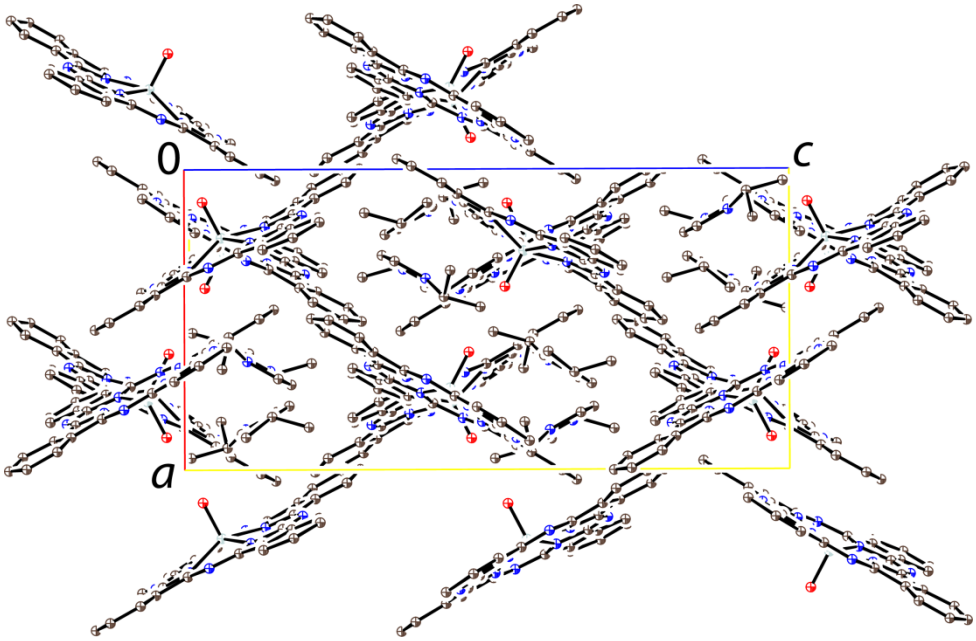

Fig. S35. View on the unit cell of salt $(i\text{-}Pr_2Im^{+})\{M^{IV}O(Pc^{\bullet 3-})\}^{\bullet -}\cdot 0.75C_6H_4Cl_2$ (**9**) along the crystallographic *b* axis.

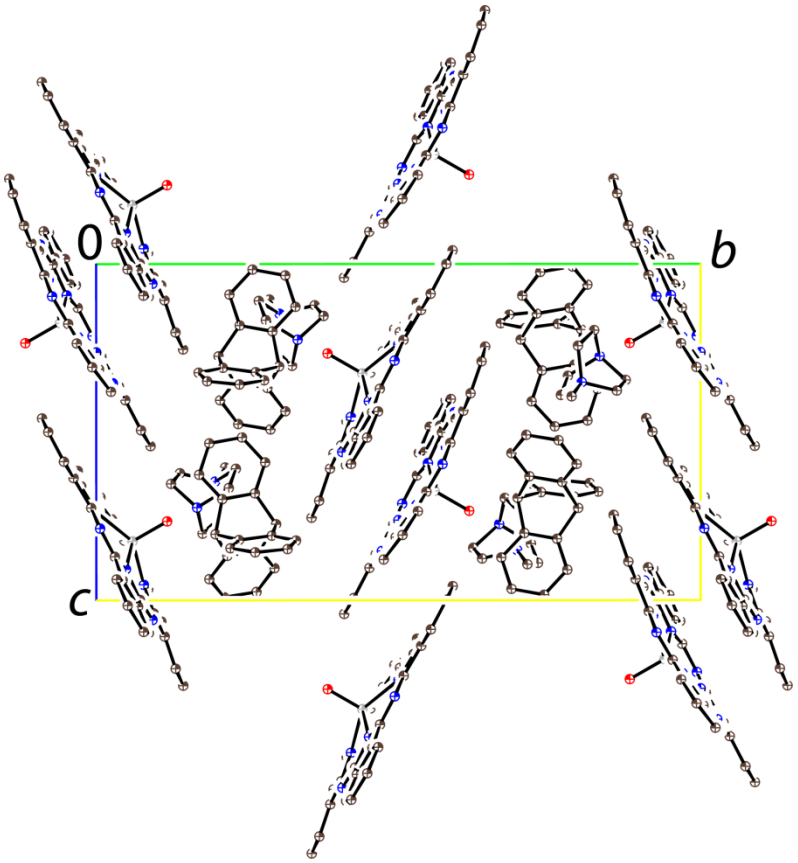

Fig. S36. View on the unit cell of salt $(MDABCO^{+})(TPC)\{M^{IV}O(Pc^{\bullet 3-})\}^{\bullet -}$ (**12**) along the crystallographic *a* axis.

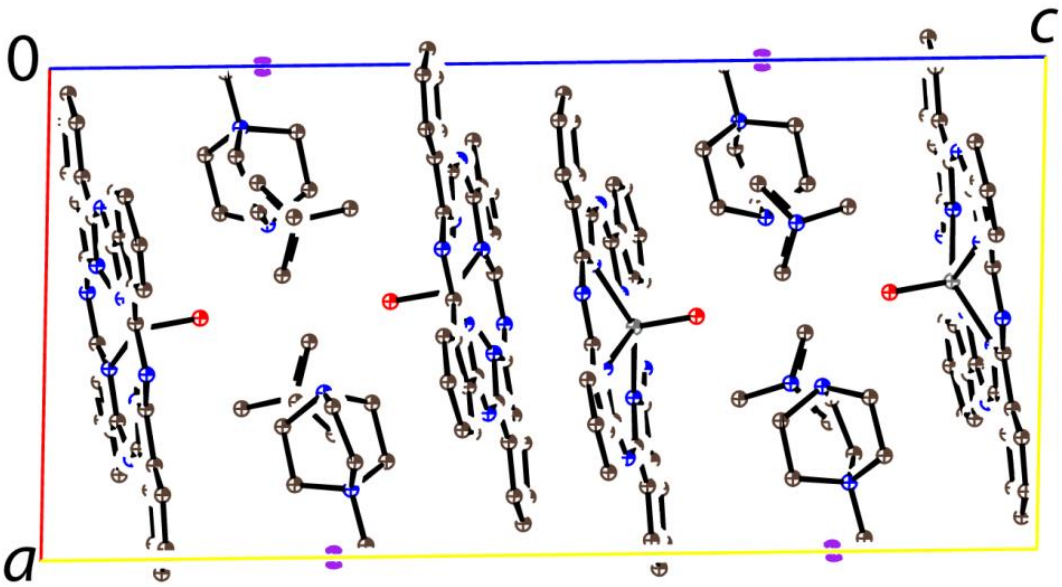

Fig. S37. View on the unit cell of salt $(MDABCO^{+})_2\{Ti^{IV}O(Pc^{\bullet 3-})\}^{\bullet -}(I^{-})$ (**13**) along the crystallographic *b* axis.

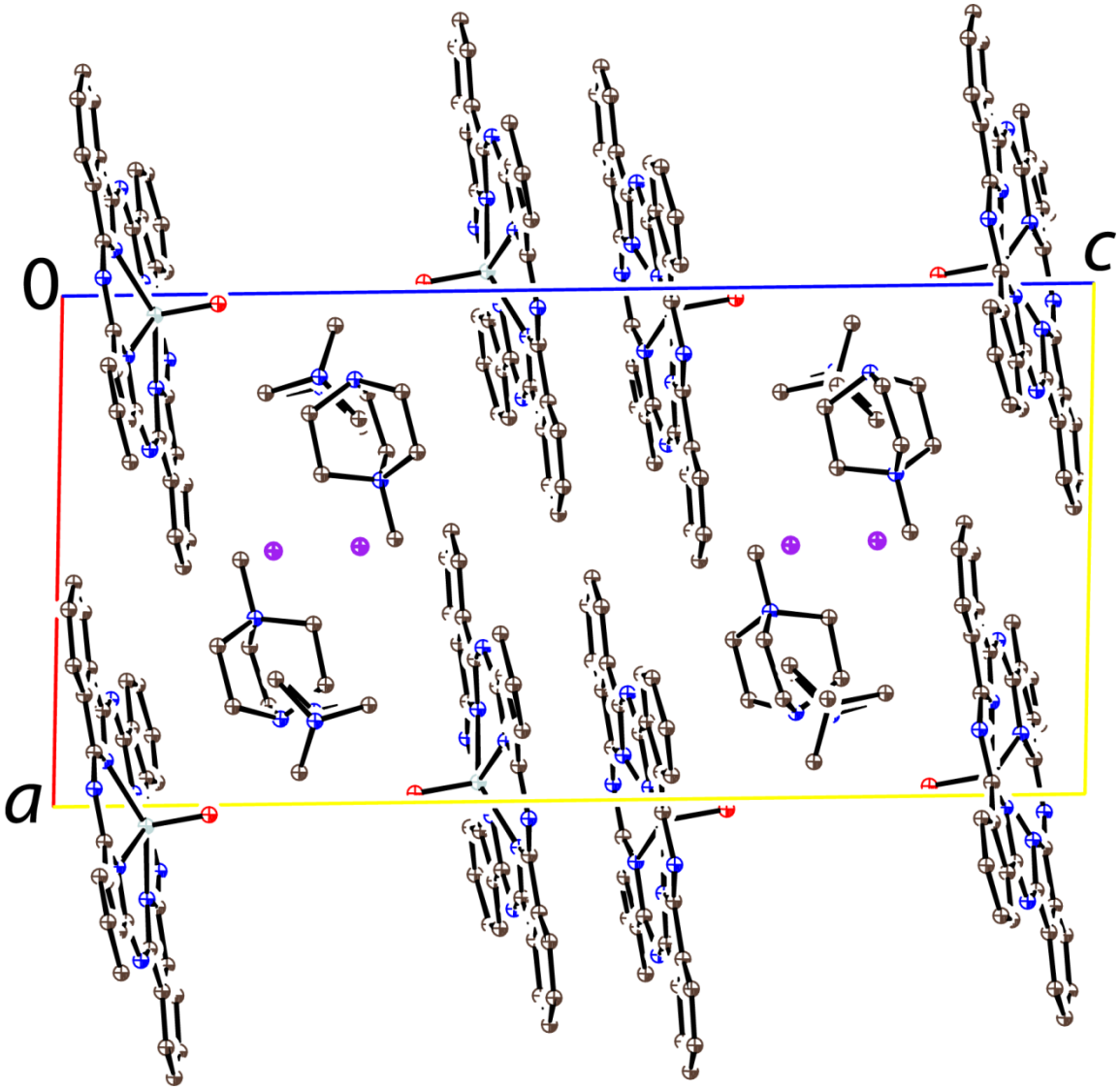

Fig. S38. View on the unit cell of salt $(MDABCO^{+})_2\{V^{IV}O(Pc^{\bullet 3-})\}^{\bullet -}(I^{-})$ (**14**) along the crystallographic *b* axis.